

Observing Topological Insulator Phases with a Programmable Quantum Simulator

Or Katz^{1,*,\dagger}, Lei Feng^{1,2,*,\ddagger}, Diego Porras³, Christopher Monroe¹

¹*Duke Quantum Center, Department of Physics and Electrical and Computer Engineering, Duke University, Durham, NC 27701*

²*Department of Physics, Fudan University, 200433 Shanghai, China*

³*Instituto de Física Fundamental (IFF), CSIC, Calle Serrano 113b, 28006 Madrid, Spain*

* These authors contributed equally.

^{\dagger}E-mail: or.katz@duke.edu

^{\ddagger}E-mail: leifeng@fudan.edu.cn

(Dated: January 22, 2024)

Topological insulators exhibit fascinating properties such as the appearance of edge states protected by symmetries. The Su-Schrieffer-Heeger (SSH) model is a canonical description of a one-dimensional quantum topological insulator. We experimentally implement a modified SSH model with long-range interacting spin systems in one-dimensional trapped ion crystals of up to 22 spins. An array of tightly focused laser beams generates site-specific Floquet fields that control the bond dimerization of the spins, which when subject to reflection symmetry, exhibit signatures of topologically-protected edge states. We study the evolution of highly excited configurations with various ranges of the spin-spin interaction, revealing the nontrivial role of many-body fermionic-interaction terms on the resulting dynamics. These results allow direct quantum simulations of topological quantum degrees of freedom expected in exotic materials, but here with high control of individual spins and their interaction range.

Topological quantum materials have triggered extensive interest in physics and materials science [1] and have potential applications as robust information carriers in quantum information science [2]. Topological insulators serve as prime examples of such materials and give rise to macroscopic properties that qualitatively differ between the material’s bulk and its edges, impacting phenomena such as quantum coherence of excitations and transport [3, 4]. Perhaps the simplest instance of a topological insulators is the Su-Schrieffer-Heeger (SSH) model in one dimension [5–7], describing a crystal of fermions with alternating bond strengths under a chiral symmetry which supports long-lived edge states.

The characterization of topological insulators is well established in electronic systems at the single-particle level. Quantum simulators based on photonic or atomic systems allow the probing of novel effects arising from the interplay between topology and dissipation and interactions. Topological insulator phases have been implemented with ultracold atoms [8, 9], photonic lattices [10–12] and Rydberg atoms [13]. Here, we implement a modified SSH model of a topological insulator in a spin-system composed of an array of trapped atomic ions, allowing the control of the range of interactions and the direct preparation and measurement of ground and excited states at the single spin level.

Trapped ion crystals are pure quantum materials that facilitate the bottom-up construction of crystals in one or higher dimensions through strong electromagnetic confinement and laser-cooling of individual atoms [14–16]. Laser-driven optical dipole forces couple the internal spin levels of different atoms with their collective

modes of motion, enabling the control of spin-spin interactions that can be long- or short-ranged, uniform or staggered in sign [17, 18]. A simple global optical dipole force allows the quantum simulation of a diverse array of quantum phases of matter, including ferromagnetic, antiferromagnetic, disordered ‘XY’, and continuous symmetry breaking phases [17, 19, 20].

Floquet engineering with optical fields, or the periodic optical driving of a material, enables further control of microscopic interaction terms and the shaping of band structures in various materials [21–25]. Indeed, Floquet Topological Insulators are materials that acquire their topological properties solely through the illumination of light. However, its practical application in solid-state systems presents experimental challenges, owing to the small length scale of the crystal and the required intensity. Floquet fields have been employed in trapped-ion and other atomic systems to create time crystals [26, 27] or investigate dynamical gauge fields [28]. However, the global nature of the applied fields in these cases has limited the complexity of the resulting model.

Here, we use a fully universal quantum computer system, with individual optical control of each spin for a site-dependent Floquet drive, to implement the SSH model [29]. We experimentally explore the topological properties of trapped-ion crystals that emerge in the presence of Floquet fields with arbitrary initial spin configurations. Using an array of optical fields that simultaneously address each individual atom in the crystal, we gain precise control over the amplitude and phases of the Floquet fields across the crystal, introducing reflection symmetry to the interaction bonds. We observe the

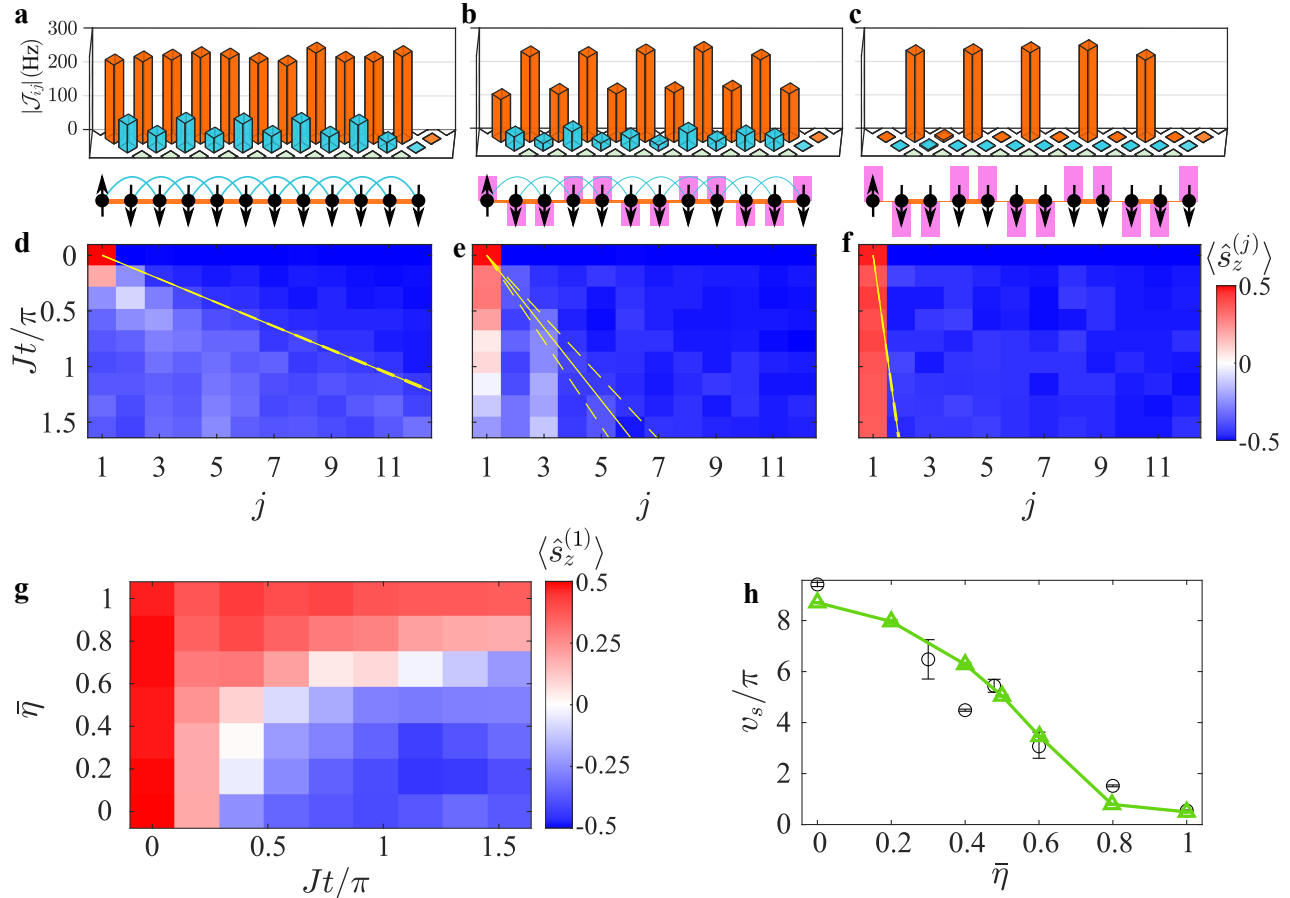


Figure 1. **Floquet Engineering of Spin Bonds and Topological Edge-States.** **a-c**, Bond dimerization in an $L = 12$ spin crystal. Measured spin-spin bond strength $\hbar|\mathcal{J}_{ij}|$ between i th and j th spins up to next-nearest neighbors (NNN) with increasing Floquet amplitude $\bar{\eta}$. **a**, No modulation ($\bar{\eta} = 0$). **b**, Moderate modulation ($\bar{\eta} = 0.6$). **c**, Full modulation ($\bar{\eta} = 1$). Black spheres for spins and lines for bonds strength, pink rectangles for local Floquet fields. **d-f** Evolution of a Single spin excitation at the edge over time for configurations **a-c** respectively. The Floquet field suppresses thermalization into the bulk, leading to edge localization. $\hbar J$: average nearest-neighbor spin bond energy absent the Floquet drive; yellow lines show excitation spreading rate (See Method). **g**, spin excitation at the crystal edge $\langle \hat{s}_z^{(1)} \rangle$ with varying Floquet field amplitude. **h**, Excitation spreading rate (black bars) slowing with increasing Floquet field amplitude, in agreement with model (green). Data in **d-h** aligns with the numerical spin model in [Extended Data Fig. 1](#).

emergence of protected excitations at the edges of one-dimensional crystals containing up to 22 spins, in contrast to the observed thermalization of the bulk. Additionally, we investigate the dynamics and thermalization rate of states comprising single and multiple spin excitations. By controlling the range of interaction while respecting the topological class of the system, we explore nontrivial extensions of the SSH model. The ability to initialize the system with site-specific spin excitations and probe their evolution allows the study the competition between interaction terms in the fermionic representation and the topological properties of the system associated with the free-fermionic Hamiltonian. These findings represent a significant advancement in the ma-

nipulation of quantum phases of matter and open up new avenues for exploring topological properties within quantum systems.

The trapped-ion crystals under investigation consist of $^{171}\text{Yb}^+$ ions, with either $L = 12$ or $L = 22$ spins, confined within a linear Paul trap on a chip [30–32]. Each ion possesses an effective spin created from two “clock” levels within its electronic ground-state ($|\uparrow_z\rangle \equiv |F = 1, M = 0\rangle$ and $|\downarrow_z\rangle \equiv |F = 0, M = 0\rangle$) [33]. Our approach involves the use of an equally-spaced array of tightly focused laser beams, in conjunction with an orthogonal global beam. This combination enables the simultaneous driving of Raman transitions between the spin states of individual ions. The Raman addressing

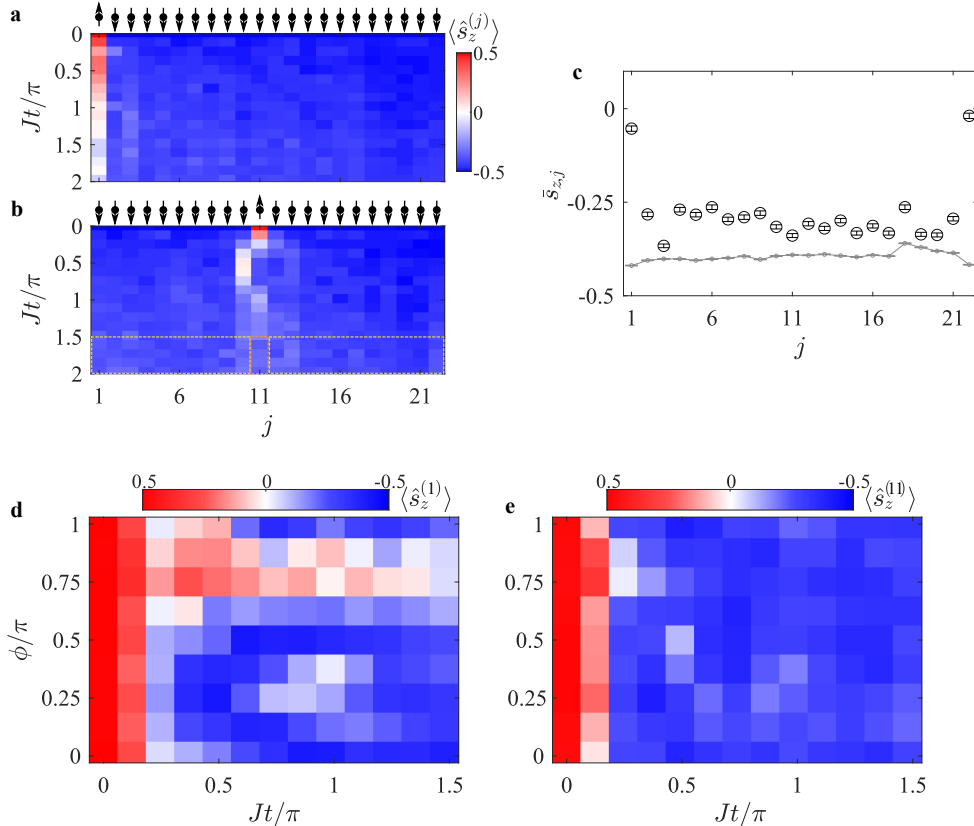


Figure 2. Edge States in a $L = 22$ Spin Crystal. Evolution of a single spin-excitation in a strongly-dimerized ($\bar{\eta} = 0.8$) crystal of $L = 22$ spins. **a** edge-excitation ($j = 1$) and, **b** bulk-excitation ($j = 11$). We repeat these experiments for all $1 \leq j \leq 22$ single-spin excitations, and for each calculate the late-time-averaged spin $\bar{s}_{z,j}$ excitation by averaging the values in the orange rectangle; see [Extended Data Fig. 2](#). **c** Late-time-averaged $\bar{s}_{z,j}$ highlights the protection of edge excitations over the bulk. Grey line shows the mean late-time excitation in all crystal sites, as calculated e.g., in the yellow box in **b**. **d-e** Evolution of Edge excitation ($j = 1$, **d**) and bulk excitation ($j = 11$, **e**) as a function of the global Floquet phase shift ϕ . **d** The edge shows greater protection at $\phi = \frac{\pi}{4}$ and $\phi = \frac{3\pi}{4}$ where the Hamiltonian features a reflection symmetry leading to Zak phase quantization and topologically protected (quasi-) zero-energy modes. Maximal protection is observed for $\phi = \frac{3\pi}{4}$ for which the Hamiltonian has a nontrivial topological phase. **e** The bulk excitation is minimally-affected by the Floquet phase.

method is attuned to the motion along the wavevector difference between the individual and global addressing Raman beams and generates a spin-spin interaction Hamiltonian mediated via the collective motional modes of the ion chain. We initialize and measure the spins using optical pumping and state-dependent fluorescence techniques [33], and the collective motional modes of the ion chain are initialized to near their ground state through sideband cooling [34].

The spin interaction we implement takes the form of an effective long-range XY Hamiltonian, with interaction bond matrix J_{ij} between spins i and j whose range is controlled (see Methods) [17]. We first render the spin bonds between nearest-neighboring spins nearly uniform, by controlling the local laser amplitudes at each ions, correcting for the non-uniform participation of ions in the driven phonon modes (see Methods).

We then control the dimerization between the spins by introducing periodic Floquet fields that manifest as site-dependent transverse magnetic fields $B_z^{(j)}(t)$ oscillating at frequency ω and with a local site-dependent phase φ_j and scaled amplitude $\bar{\eta}$ (see Methods). These Floquet fields modify the spin-spin Hamiltonian and in the high-frequency limit $\omega \gg |J_{ij}|$ suppress bonds between spins driven by unequal local field amplitudes between sites i, j where $\varphi_i \neq \varphi_j$. This results in an effective static Hamiltonian, given by ($\hbar = 1$)

$$H = \sum_{i,j} \mathcal{J}_{ij} \left(\hat{s}_+^{(i)} \hat{s}_-^{(j)} + \hat{s}_-^{(i)} \hat{s}_+^{(j)} \right) \quad (1)$$

where \mathcal{J}_{ij} represents the transformed coefficient dressed by the Floquet field, and $\hat{\mathbf{s}}^{(j)}$ are the spin- $\frac{1}{2}$ operators of the j -th ion.

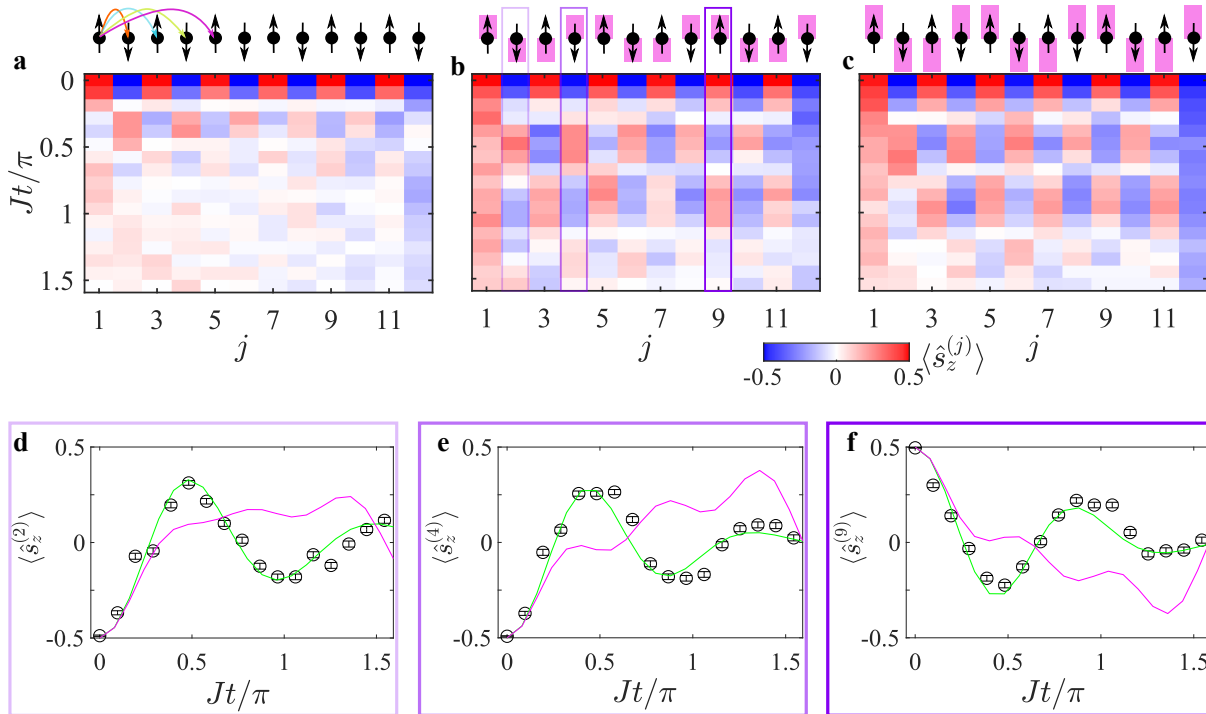


Figure 3. **Signatures of Fermionic Interaction terms.** Evolution of a $L = 12$ spin crystal with long-range interactions, initialized in a staggered spin state. **a**, In the absence of Floquet fields ($\bar{\eta} = 0$), the spin excitations quickly hop and thermalize. With full Floquet modulation (**b**, $\bar{\eta} = 0.6$ and **c**, $\bar{\eta} = 1$), thermalization is partially suppressed and the edges become more protected. **d-f** Simulation of the $\bar{\eta} = 0.6$ configuration (subplot **b**) of spins $j = 2$ (**d**), $j = 4$ (**e**) and $j = 9$ (**f**). Experimental data (black circle with errorbar) agree well with a full simulation of an equivalent fermionic Hamiltonian containing interaction terms (green curve), but not with a long-range free-fermionic Hamiltonian (magenta curve). These results are contrasted with short range spin models which are fully explained by free-fermionic evolution. See text and [Extended Data Fig. 3](#).

We apply a periodic phase pattern $\varphi_j = \frac{\pi}{2}j + \phi$ for $1 \leq j \leq L$, and this structure renders the Hamiltonian in Eq. (1) reflection symmetric and induces a nontrivial topological phase for $\phi = \frac{3\pi}{4}$ (see Methods). In Fig. 1a-c, we display the measured bond matrices for a $L = 12$ crystal for different amplitudes of the Floquet drive; see Methods for details of the bond-strength measurement. Increasing the Floquet drive from $\bar{\eta} = 0$ to $\bar{\eta} = 1$ effectively suppresses the odd bonds in comparison to the even ones, allowing for control over the dimerization of bonds in the chain.

We first examine the effects of Floquet dressing on a solitary spin excitation positioned at the edge of the crystal. In Figs. 1d-f, we present the measured evolution dynamics of each spin $\langle \hat{s}_z^{(j)}(t) \rangle$ governed by the Hamiltonian in Eq. (1) for a crystal comprising $L = 12$ spins, all oriented downwards, except for the spin at edge $j = 1$ that is aligned upwards along the spin z -axis. The temporal progression is normalized with respect to the mean nearest-neighbor bond strength J in the absence of the Floquet drive. In the absence of the Floquet field ($\bar{\eta} = 0$), the spin excitation tends to ther-

malize with the chain over time, as illustrated in Fig. 1d. With an increase in the strength of the Floquet field ($\bar{\eta} = 0.6$, Fig. 1e), the process of thermalization noticeably decelerates. When the chain is fully dimerized with $\bar{\eta} = 1$, the spin excitation remains confined to the edge and ceases to thermalize, as exemplified in Fig. 1f. We present the edge spin's magnetization quantitatively as a function of the drive's amplitude in Fig. 1g. Additionally, we present the excitation spreading rate in Fig. 1h, which is extracted from the slope of the yellow solid lines shown for instance in Fig. 1(d-f) (see Methods). The measured values align closely with a theoretical model, computed numerically via the Unitary evolution of the spins, as displayed in [Extended Data Fig. 1\(a-e\)](#). Further details regarding the theoretical model can be found in the Methods section.

A key characteristic of topological insulators is the distinct response of excitations at the edges compared to those within the crystal's bulk. We repeated our experiment using a strongly dimerized crystal ($\bar{\eta} = 0.8$) with $L = 22$ spins and a longer interaction range; see Methods for experimental details. We considered all

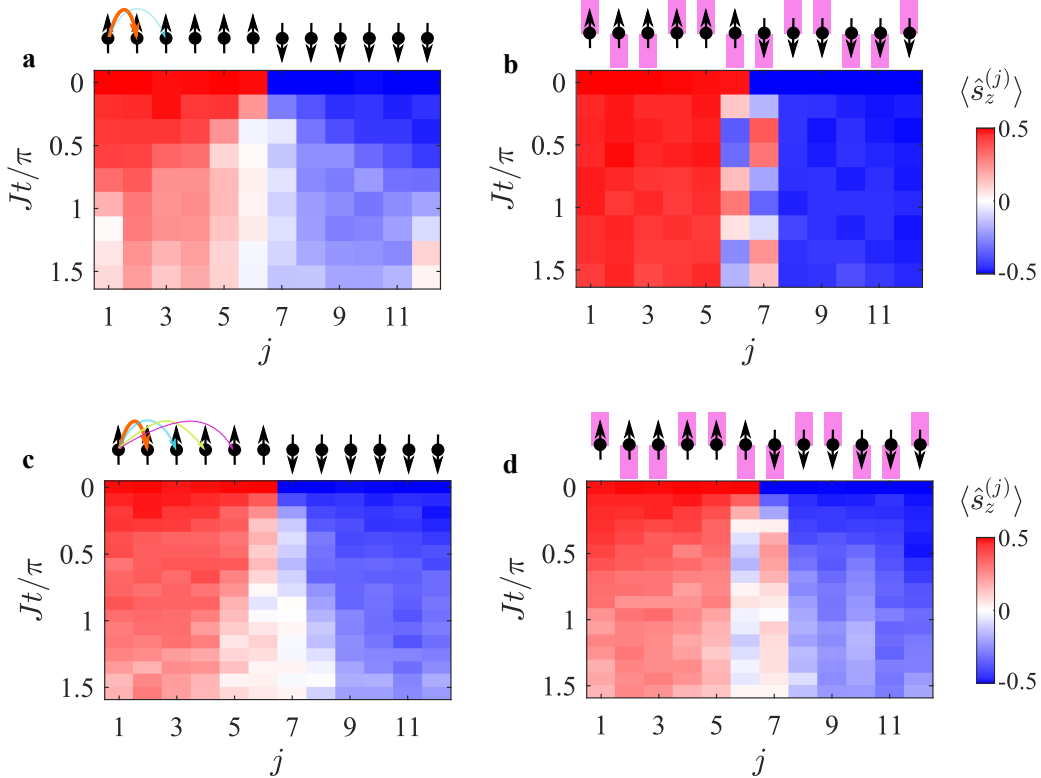


Figure 4. **Domain wall dynamics.** The evolution of two domain walls in a $L = 12$ spin crystal, comprising of multiple spin-excitations. **a-b** Short range spin-spin interaction, and **c-d** Long-range spin-spin interaction. **a,c** Absent the Floquet field ($\bar{\eta} = 0$), the domain walls thermalize as excitations are free to hop. **b,d** Fully dimmerized crystal ($\bar{\eta} = 1$). **b** Boundary excitations between the walls are exchanged coherently, and the domain walls maintain their state in **b** or partially thermalize in **d**. The results in **a-d** agree well with numerical calculation of the spin evolution, see [Extended Data Fig. 4](#).

possible configurations of single-spin excitations at sites $1 \leq j \leq 22$ as shown in [Extended Data Fig. 2](#) and Fig. 2a ($j = 1$) and Fig. 2b ($j = 11$). Our findings reveal that while bulk excitations rapidly thermalize, edge excitations feature greater isolation. To quantify this difference, we calculated the late time-averaged magnetization of each excited spin at site j , denoted as $\bar{s}_{z,j} = 2 \int_{1.5}^2 \langle \hat{s}_z^{(j)}(\tau) \rangle d\tau$, with $\tau = Jt/\pi$, as depicted in Fig. 2c. In comparison, dash line denotes the measured late-time-averaged excitation of the crystal, \bar{s}_z , averaged over all crystal sites. The enhanced persistence of spin excitations at the edges ($j = 1$ or $j = 22$), compared to the bulk of the crystal ($2 \leq j \leq 21$), serves as a distinctive hallmark of the crystal's topological state.

The observed protection of spins near the edges originates from the topological structure induced by the Floquet fields. To investigate this, we probe the magnetization of the initially excited spin as a function of the global phase of the Floquet fields ϕ , while maintaining a fixed modulation amplitude $\bar{\eta} = 0.8$ for the $L = 22$ crystal. In Fig. 2d, we study a single edge excitation ($j = 1$), finding maximal protection at $\phi = \frac{3\pi}{4}$, the value at which the Hamiltonian becomes reflection symmet-

ric, the Zak phase is quantized with a nonzero value, and the topological phase is expected to be nontrivial [29] (see Methods). In contrast, the evolution of a spin within the bulk (with $j = 11$), as shown in Fig. 2e, is barely affected, rapidly losing the excitation for all values of ϕ . These results underscore the significance of the site-dependent pattern of the Floquet field and the reflection symmetry that imparts topological properties to the Hamiltonian.

Our ability to manipulate the spin states and the range of interactions offers opportunities for exploring topological and dynamics beyond single-spin excitation. In Fig. 3(a-b), we depict the evolution of an $L = 12$ spin crystal initialized in a Néel state, where spins at odd (even) lattice sites point upwards (downwards). Here we set the spin-spin interaction range to be long-range (see Methods). While absent the Floquet fields ($\bar{\eta} = 0$) all spin excitations thermalize rapidly (Fig. 3a), in the presence of Floquet fields ($\bar{\eta} = 0.6$ in Fig. 3b and $\bar{\eta} = 1$ in Fig. 3c) the thermalization of excitations greatly slows down, predominantly near the edges of the crystal.

To interpret this multi-excitation dynamics and associate it with the role of fermionic interaction, we com-

pare the experiment's dynamics under two models. The first model involves a complete fermionic representation of the Hamiltonian as defined in Eq. (1). The second model considers free fermionic evolution with long-range effects by removing fermionic interaction terms (see Methods). We observe qualitatively different behavior between these two models while finding a strong agreement between the measured data and the exact model, as exemplified in Fig. 3(d-f). This finding underscores the importance of interaction terms in the dynamics. These terms enhance thermalization and oppose topological protection, although they do not eliminate it. To further highlight these findings, we replicate these measurements and analyses for a crystal with short-range interactions, as shown in [Extended Data Fig. 3](#). In this case, we observe good qualitative agreement with the free fermionic model, in line with the expectations of the standard SSH model- a free fermionic model.

Before concluding, we present another intriguing multiple-excitation scenario where the spin excitations are ordered to form two domain walls. The left half of the $L = 12$ crystal are oriented upwards and those in the right half point downwards. As we increase the amplitude of the Floquet drive ($\bar{\eta} = 0$ in **a**, $\bar{\eta} = 1$ in **b**), for a short-range interacting crystal, we observe the suppression of thermalization of the two domain walls and the exchange of excitations between the spins at the boundary becomes evident. This result qualitatively agrees with the SSH model, which assumes nearest-neighbor interactions. Performing the same experiment for a bond matrix with a significantly longer interaction range ($\bar{\eta} = 0$ in **c**, $\bar{\eta} = 1$ in **d**) yields qualitatively different results. We observe a combination of thermalization and boundary excitation, attributed to the bonding of distant spins. These experimental results align well with our numerical spin model, as shown in [Extended Data Fig. 4](#). The dynamics of the domain walls are explained by the coherent oscillation between the initial state and the edge-states at the boundary of each of the two domains, as the interaction matrix element between those states dominates over the coupling to the bulk (see Methods). Our experimental results thus demonstrate, for the first time, the creation of edge states around a boundary set by the initial state rather than system parameters.

In summary, we present an investigation into the topological properties of a trapped-ion crystal, leveraging optical Floquet fields with single-atom resolution within the crystal. Our study encompasses an exploration of thermalization and the protection of single-spin excitations, highlighting the notably distinct behavior at the crystal's edges compared to the bulk. Furthermore, we explore the role of the topological structure controlled by the spatial phase of the periodic drive. In addition, our examination of multiple excited states, subject to varying ranges of interaction, provides means

for studying the delicate balance between many-body interactions and their influence on the topological nature of the Hamiltonian.

This work opens up new avenues for investigating topological quantum phases of matter in low-dimensional systems, for example by studying many-body ground states and spin-wave interactions. Our trapped ion simulator allows to use an interacting spin system both with tunable long-range interactions and quantum effects, thus addressing some of the limitations found in other photonic or atomic platforms. Furthermore, the possibility to prepare and measure quantum states at the single-site level permits to study topological effects arising from dynamics of non-trivial initial states.

ACKNOWLEDGMENTS

We thank Marko Cetina, Victor Gurarie, Pedro Nevado and Alvaro Gomez for fruitful discussions. This work is supported by the U.S. Department of Energy, Office of Science, National Quantum Information Science Research Centers, Quantum Systems Accelerator. Additional support is acknowledged from the NSF STAQ Program, the NSF QLCI Center on Robust Quantum Simulations, the AFOSR MURI on Dissipation Engineering in Open Quantum Systems, and the Spanish project PID2021-127968NB-I00 funded by MCIN/AEI/10.13039/501100011033/FEDER, UE.

Methods

ADDITIONAL EXPERIMENTAL DETAILS

We implement the long-range XY Hamiltonian by applying the Ising spin-spin interaction Hamiltonian H_{XX} in the presence of a large transverse magnetic field Hamiltonian H_Z . The Ising term is generated via Raman transitions mediated by pairs of beams, which virtually excite collective motion of the ions. One optical beam passes through an acousto-optical modulator (AOM). The AOM is simultaneously driven by two radio-frequency (RF) signals, which split the optical beam into two components with distinct frequencies. These components are then imaged onto the ion chain to address all ions globally. Another beam is split into an array of more than thirty tightly focused beams, passing through a multi-channel AOM. Twenty-two independent RF signals control the frequency and amplitude of 22 beams, with all other beams being blocked. This combination concurrently drive the first red and blue sideband transitions in the dispersive regime, with nearly symmetric detunings from the radial collective motional modes. This configuration realizes the Ising Hamiltonian $H_{XX} = 2 \sum_{i,j}^L J_{ij} \hat{s}_x^{(i)} \hat{s}_x^{(j)}$ with a symmetric spin-spin interaction matrix J_{ij} [17].

The J_{ij} matrix we realize can be calculated through [17, 20]

$$J_{ij} = \sum_{k=1}^N \frac{\eta_{ik} \eta_{jk} \Omega_i \Omega_j}{2(\Delta + \omega_N - \omega_k)}. \quad (2)$$

Here, $\eta_{ik} = 0.08 b_{ik}$ are the Lamb-Dicke parameters describing the coupling between spin i and motional mode k through the Raman transitions, with b_{ik} as the mode participation matrix elements [32]. Ω_j denotes the resonant carrier Rabi frequency at ion $1 \leq j \leq L$ for each tone, and ω_k represents the motional frequencies along one radial direction, labeled in decreasing order with $1 \leq k \leq N$. The $L = 12$ ($L = 22$) spin crystal is constructed using the middle ions in a chain of $N = 15$ ($N = 27$) atoms, with $N - L$ auxiliary ions located near the edges of the chain¹. These auxiliary ions participate in collective motion via their Coulomb coupling to the other ions, but are not illuminated by the Raman beams (i.e. their equivalent Ω_j is set to zero). Consequently, the evolution is independent of the auxiliary ions' spins,

as their J_{ij} matrix elements are identically zero, and they are not considered as part of the spin crystal described in the main text. Their presence contribute to increasing the trapping potential near the edges of the crystal, ensuring nearly uniform spacing between the L inner ions, with an average distance of approximately $3.75 \mu\text{m}$. This uniformity is crucial for aligning with the uniformly-spaced array of individually addressing beams.

The trap frequencies and mode participation factors are determined by the trapping potential. We employ a quadratic trapping potential in the radial direction with center-of-mass frequency of $\omega_1 = 2\pi \times 3.08$ MHz and an axial electrostatic potential of $V(x) = c_4 x^4 + c_2 x^2$. For the 15-ion chain, the coefficients are $c_2 = 0.11, \text{eV}/\text{mm}^2$ and $c_4 = 1.6 \times 10^3, \text{eV}/\text{mm}^4$, while for the 27-ion chain, they are $c_2 = -0.1, \text{eV}/\text{mm}^2$ and $c_4 = 235, \text{eV}/\text{mm}^4$. Here, x is the coordinate along the chain axis. These potentials determine the frequencies of the collective modes of motion. The effective wave-vector of the optical field is aligned to selectively drive only one specific set of radial modes. For the $N = 15$ ion chain, the frequencies are $\omega_k \in \{3.08, 3.07, 3.05, 3.03, 3.01, 2.98, 2.96, 2.93, 2.90, 2.88, 2.85, 2.83, 2.80, 2.78, 2.78 | 1 \leq k \leq 15\}$ MHz. In the case of the $N = 27$ ion chain, the frequencies of the collective motional modes are as follows: $\omega_k \in \{3.08, 3.07, 3.07, 3.06, 3.05, 3.04, 3.03, 3.02, 3.00, 2.99, 2.98, 2.96, 2.95, 2.93, 2.92, 2.90, 2.89, 2.87, 2.86, 2.84, 2.83, 2.82, 2.81, 2.80, 2.79, 2.77, 2.77 | 1 \leq k \leq 27\}$ MHz.

We control the range of interaction of the realized J_{ij} matrices by adjusting the Raman beat-note detuning Δ , which is measured relative to the transition of the least-frequency radial (zig-zag) motional mode. We further achieve relatively uniform spin bonds (absent the Floquet field) through control of the individual beams' amplitudes, compensating for the rapid spatial variation of the low-frequency phonon modes participation matrix elements. In this work, we implemented three different interaction matrices. The first interaction matrix J_{ij} , calculated using Eq. (2) for the $L = 12$ spin crystal ($N = 15$ ion chain) is depicted in [Extended Data Fig. 5a](#). It was achieved with $\Delta = -99$ kHz, $J = 0.25$ kHz and by normalizing the beams' amplitudes in the array to follow $\Omega_j/\Omega_1 = \{1.0, 1.0, 0.65, 0.87, 0.69, 0.97, 0.74, 0.97, 0.68, 0.86, 0.65, 0.99 | 1 \leq j \leq 12\}$. This configuration results in a short-range interaction matrix, which decays approximately exponentially and is staggered in its sign, as expected from detuning near the zig-zag mode [18]. We estimated the average bond strength between spins i and j as $\bar{J}(d) = \frac{1}{L-d} \sum_{n=1}^{L-d} |J_{n,n+d}|$ where $d = |i - j|$ represents the distance between the two spins. The calculated $\bar{J}(d)$ is presented in [Extended Data Fig. 5d](#) (diamonds) and fitted with a curve $\bar{J}(d) = 3.9J \times e^{-1.36|i-j|}$. This experimental configuration was used in generating [Fig. 1](#), [Fig. 4a-b](#), [Extended Data Fig. 1](#), [Extended Data](#)

¹ For the $N = 15$ chain, one auxiliary ion is positioned at the left end of the $L = 12$ crystal spin (site $j = 0$), and two ions are placed at the right end (sites $j = 13, 14$). In the case of the $N = 27$ chain, there are two auxiliary ions on the left side (sites $j = -1, 0$) of the $L = 22$ spin crystal, along with an additional three ions on the right edge (sites $j = 23, 24, 25$).

Fig. 3g-1 and Extended Data Fig. 4g-1.

The second interaction matrix J_{ij} for the $L = 12$ spin crystal ($N = 15$ ion chain) is illustrated in Extended Data Fig. 5b. It exhibits a longer-range interaction, with all coefficients having the same positive sign. This matrix is realized by detuning the Raman beatnote near the center of mass (COM) mode, with $\Delta = 29 \text{ kHz} + \omega_1 - \omega_N$ and $J = 0.25 \text{ kHz}$. use a relative Rabi frequency profile $\Omega_j/\Omega_1 = \{1.0, 1.0, 1.10, 1.07, 1.16, 1.10, 1.17, 1.10, 1.16, 1.07, 1.10, 1.0\} |1 \leq j \leq 12\}$ to make the nearest neighbor (NN) bonds nearly uniform in strength. The calculated $\bar{J}(d)$ is presented in Extended Data Fig. 5d (asterisks) and approximated by the curve $\bar{J}(d) = 1.5J \times e^{-0.42|i-j|}$. This configuration was used to generate Fig. 3, Extended Data Fig. 3a-f and Extended Data Fig. 4a-f.

The third configuration was employed for the $L = 22$ spin crystal ($N = 27$ ion chain) as depicted in Extended Data Fig. 5c. In this setup, we detuned $\Delta = -45 \text{ kHz}$ below the zig-zag mode, set $J = 0.2 \text{ kHz}$ and achieved relatively uniform nearest neighbor (NN) spin bonds by configuring the relative Rabi frequencies as $\Omega_j/\Omega_1 = \{1.0, 0.59, 0.59, 0.4, 0.47, 0.37, 0.50, 0.44, 0.60, 0.51, 0.68, 0.54, 0.68, 0.52, 0.62, 0.45, 0.53, 0.39, 0.49, 0.42, 0.61, 0.60\} |1 \leq j \leq 22\}$. The calculated $\bar{J}(d)$ is presented in Extended Data Fig. 5d (squares) and can be approximated by the curve $\bar{J}(d) = 2.7J \times e^{-|i-j|}$. This configuration was used in generating Fig. 2 and Extended Data Fig. 2.

Simultaneously with the Ising interaction, we apply the transverse magnetic field Hamiltonian $H_Z = \sum_{j=1}^L B_z^{(j)} \hat{s}_z^{(j)}$ [17, 20]. We achieve independent control over the the local magnetic field affecting each spin by shifting the optical frequency of the individually-addressing beam using its AOM channel. Since the spin is measured relative to the laser rotating frame, an instantaneous shift of the optical frequency of the j th beam by $B_z^{(j)}(t)$ Hz relative to the carrier transition is equivalent to the application of such a transverse magnetic field in the spin frame. We shift and modulate the optical frequency to generate the magnetic fields that take the form

$$B_z^{(j)}(t) = B_0 + \bar{\eta} \frac{z_0 \omega}{\sqrt{2}} \cos(\omega t) \cos(\varphi_j), \quad (3)$$

where $z_0 \approx 2.4$ is the first root of the 0th Bessel function of the first kind. We experimentally set $B_0 = 18J$ and $\omega = 6J$ for all configurations. To ensure that this magnetic field is applied correctly, we independently calibrate for light-induced shifts generated by the Raman light, and compensate for them by shifting the optical frequency of each individually-addressing beam in the array. We also ensure that the amplitudes of the red and blue tones are balanced, to minimize light shift noise in the presence of the Ising interaction.

We measure each J_{ij} element in Fig. 1a-c by turning on the two beams addressing the i th and j th ions while

turning off all other beams in the array. The ions are initialized in the state $|\uparrow_z^{(i)} \downarrow_z^{(j)}\rangle$ for $j > i$. Unlike Ref. [20], here, the magnetic field in Eq. (3) is applied during the measurement, along with a constant-amplitude pulse, and oscillations in the populations are measured. We fit the average staggered magnetization $\langle \hat{s}_z^{(i)} - \hat{s}_z^{(j)} \rangle$ to the function $\exp(-\Gamma_{ij} t) \cos(\pi J_{ij} t)$ using J_{ij} and Γ_{ij} as fitting parameters.

DIMMERIZATION OF BONDS BY THE FLOQUET DRIVE

The transverse field Ising model under consideration is effectively described by the Hamiltonian in Eq. (1). This representation is achieved through a frame transformation that rotates each spin by its Larmor frequency corresponding to its local transverse field. Given that the applied transverse fields dominate the Ising interaction ($B_z^{(j)} \gg \bar{J}$), we can express it as the Ising Hamiltonian using the raising and lowering spin operators $\hat{s}_x^{(i)} \hat{s}_x^{(j)} \approx \frac{1}{2}(\hat{s}_+^{(i)} \hat{s}_-^{(j)} + \hat{s}_-^{(i)} \hat{s}_+^{(j)})$. This transformation introduces fast oscillations to the terms involving $\hat{s}_\pm^{(i)} \hat{s}_\pm^{(j)}$ [17].

The periodic drives applied to the system modify the bare spin interaction matrix J_{ij} and yield a scaled interaction matrix \mathcal{J}_{ij} [29].

$$\mathcal{J}_{ij} = j_0 \left(2\eta \sin\left(\frac{\pi}{4}(i+j) + \phi\right) \sin\left(\frac{\pi}{4}(i-j)\right) \right) J_{ij}. \quad (4)$$

Here, $j_0(x)$ denotes the 0th Bessel function of the first kind and $\eta = \frac{z_0 \bar{\eta}}{\sqrt{2}}$. At values of $\phi = \frac{\pi}{4}$ and $\phi = \frac{3\pi}{4}$ edge-states are topologically protected by inversion symmetry, and the Zak phase of the long-range SSH model is quantized [29]. Therefore, we specifically focus our discussion on these particular points.

The topological properties of our model become evident when we explicitly define the sub-lattice structure. We assume that N is even and divide the chain into odd (A sublattice) and even sites (B sublattice), as illustrated in Fig. Extended Data Fig. 6. We express the $N \times N$ interaction matrix \mathcal{J}_{ij} in terms of four $N/2 \times N/2$ sub-matrices, with elements denoted as $\mathcal{J}_{An;Am}$, $\mathcal{J}_{Bn;Bm}$, $\mathcal{J}_{An;Bm}$, $\mathcal{J}_{Bn;Am}$. Here $\mathcal{J}_{An;Bm}$ denotes the coupling between site n in sublattice A, and site m in sublattice B, and so on. For values $\phi = \frac{\pi}{4}$, $\frac{3\pi}{4}$, we obtain

$$\mathcal{J}_{An;Am} = \mathcal{J}_{Bn;Bm} = J(2d)D(d), \quad (5)$$

where $d = n - m$, and $D(d)$ is a dimerization parameter that takes the values $D(d) = j_0(0) = 1$ if d is even, and $D(d) = j_0(\bar{\eta} z_0)$ if d is odd. Equation (5) implies that the chain possesses inversion symmetry, assuming that the original non-dressed interaction is homogeneous

(i.e. $J_{nm} = J(d)$), a condition not fulfilled for values $\phi \neq \frac{\pi}{4}, \frac{3\pi}{4}$. We also have non-diagonal blocks represented by

$$\mathcal{J}_{An;Bm} = J(2d-1)\bar{D}(d), \quad (6)$$

with a different dimerization parameter $\bar{D}(d)$. If d is even, it takes values $\bar{D}(d) = j_0(0)$ for $\phi = \frac{\pi}{4}$ and $\bar{D}(d) = j_0(\bar{\eta}z_0)$ for $\phi = \frac{3\pi}{4}$. If d is odd, $\bar{D}(d) = j_0(\bar{\eta}z_0)$ for $\phi = \frac{\pi}{4}$ and $\bar{D}(d) = j_0(0)$ for $\phi = \frac{3\pi}{4}$.

The bulk properties of the system are described in the plane-wave basis with momentum k in which the dressed interaction matrix can be written in terms of the four blocks

$$\begin{aligned} \mathcal{J}(k) &= \begin{pmatrix} E(k) & \Delta(k) \\ \Delta^*(k) & E(k) \end{pmatrix} \\ &= E(k)\mathbb{1} + \Delta(k)\sigma^+ + \Delta^*(k)\sigma_-. \end{aligned} \quad (7)$$

with $E(k) = \sum_d J(2d)D(d)e^{ikd}$, and $\Delta(k) = \sum_d J(2d-1)\bar{D}(d)e^{ikd}$. The matrix $\mathcal{J}(k)$ possesses both time-reversal and inversion symmetry,

$$\begin{aligned} \mathcal{J}(k) &= \mathcal{J}(-k)^*, \\ \mathcal{J}(k) &= I\mathcal{J}(-k)^*I, \end{aligned} \quad (8)$$

with the inversion operator $I = \sigma_x$ [35–37].

In the short-range limit ($J(d) = 0$ beyond nearest-neighbors, $d > 1$), the matrix \mathcal{J}_{ij} , corresponds to the standard SSH model with $\epsilon(k) = 0$ and $\Delta(k) = J(1)(\bar{D}(0)e^{ikd} + \bar{D}(1)e^{-ikd})$. If we adiabatically deform the matrix $\mathcal{J}(k)$ by increasing the range of interactions, the number of edge states - which is a topological invariant - will be conserved. Such adiabatic deformation of $\mathcal{J}(k)$ is valid as long as the gap remains open and the symmetries of the system are preserved, a condition guaranteed at $\phi = \frac{\pi}{4}, \frac{3\pi}{4}$.

To illustrate this scenario, we consider the eigenstates of the matrix \mathcal{J} for an exponentially decaying interaction profile

$$J_{ij} = J e^{-|i-j|/\xi} \quad (9)$$

with a non-zero dimerization parameter. In the limit $\xi \ll 1$, we are in the standard short-range SSH model (see [Extended Data Fig. 7](#) for a crystal of $L = 50$ spins). Dimerization induces two zero-energy mid-gap states. By adiabatically deforming the interaction range of this Hamiltonian while keeping $\phi = \frac{3\pi}{4}$, we find that the two degenerate states survive. However, when the interaction is so long-range that the gap is too small, the conditions for adiabatic deformation are no longer met, and the edge-states merge with the bulk and disappear.

FERMIONIC REPRESENTATION

Spin SSH models can be represented in terms of free fermions, such that their dynamics is governed by single-

particle physics. Long-range terms lead to fermion-fermion interactions. This fermionic representation relies on the Jordan-Wigner transformation,

$$\begin{aligned} \hat{s}_-^{(j)} &= \frac{1}{2}\hat{c}_j e^{-i\pi \sum_{j' < j} \hat{c}_{j'}^\dagger \hat{c}_{j'}}, \\ \hat{s}_+^{(j)} &= \frac{1}{2}e^{i\pi \sum_{j' < j} \hat{c}_{j'}^\dagger \hat{c}_{j'}} \hat{c}_j^\dagger, \\ \hat{s}_z^{(j)} &= \hat{c}_j^\dagger \hat{c}_j - \frac{1}{2}. \end{aligned} \quad (10)$$

Here \hat{c}_j and \hat{c}_j^\dagger are the fermionic annihilation and creation operators in site j , respectively. The long-range spin Hamiltonian in Eq. (1) casts as,

$$H = \sum_{i,j} \hat{c}_i^\dagger \hat{\mathcal{J}}_{ij} \hat{c}_j, \quad (11)$$

with the modified interaction matrix

$$\hat{\mathcal{J}}_{ij} = \mathcal{J}_{ij} \prod_{i < j' < j} (2\hat{c}_{j'}^\dagger \hat{c}_{j'} - 1). \quad (12)$$

For the scenario of short range interactions, the spin SSH Hamiltonian is equivalent to the free fermion one, since $\hat{\mathcal{J}}_{i,i+1} = \mathcal{J}_{i,i+1}$. However, for long range interaction, spin-spin interactions $\hat{\mathcal{J}}_{i,i+r}$ with $r > 1$ include string operators that depend on the fermionic number operators at intermediate sites. This leads to many-body fermion-fermion interaction terms, rendering the Hamiltonian in Eq. (11) non-quadratic in the fermionic operators. Our numerical simulation of the long-range, free-fermionic Hamiltonian, shown in Fig. 3(d-f) is realized by solving the Evolution governed by the fermionic Hamiltonian in Eq. (11) for $\hat{\mathcal{J}}_{ij} = \mathcal{J}_{ij}$, thus neglecting the string operators that lead to fermion-fermion interactions.

DOMAIN WALL DYNAMICS

The domain wall evolution observed in Fig. 4 can be understood by expressing the interaction between and within the domains. The initial state of the spin crystal is represented as $|\psi_0\rangle = |\uparrow\rangle_1 \dots |\uparrow\rangle_{\frac{N}{2}-1} |\downarrow\rangle_{\frac{N}{2}} \dots |\downarrow\rangle_N \equiv |\uparrow\rangle_L |\downarrow\rangle_R$, and the interaction matrix is decomposed into $\mathcal{J} = \mathcal{J}_L + \mathcal{J}_R + \mathcal{J}_{LR}$. Here, \mathcal{J}_L and \mathcal{J}_R are the interaction matrix within the left-side ($j = 1, \dots, N/2$) and the right-side spins ($j = N/2 + 1, \dots, N$), respectively, and \mathcal{J}_{LR} is the interaction matrix between the left and right sides. The initial state is an eigenstate of the spin Hamiltonian corresponding to uncoupled halves, satisfying

$$\sum_{ij} (\mathcal{J}_L + \mathcal{J}_R)_{ij} \hat{s}_+^{(i)} \hat{s}_-^{(j)} |\psi_0\rangle = 0. \quad (13)$$

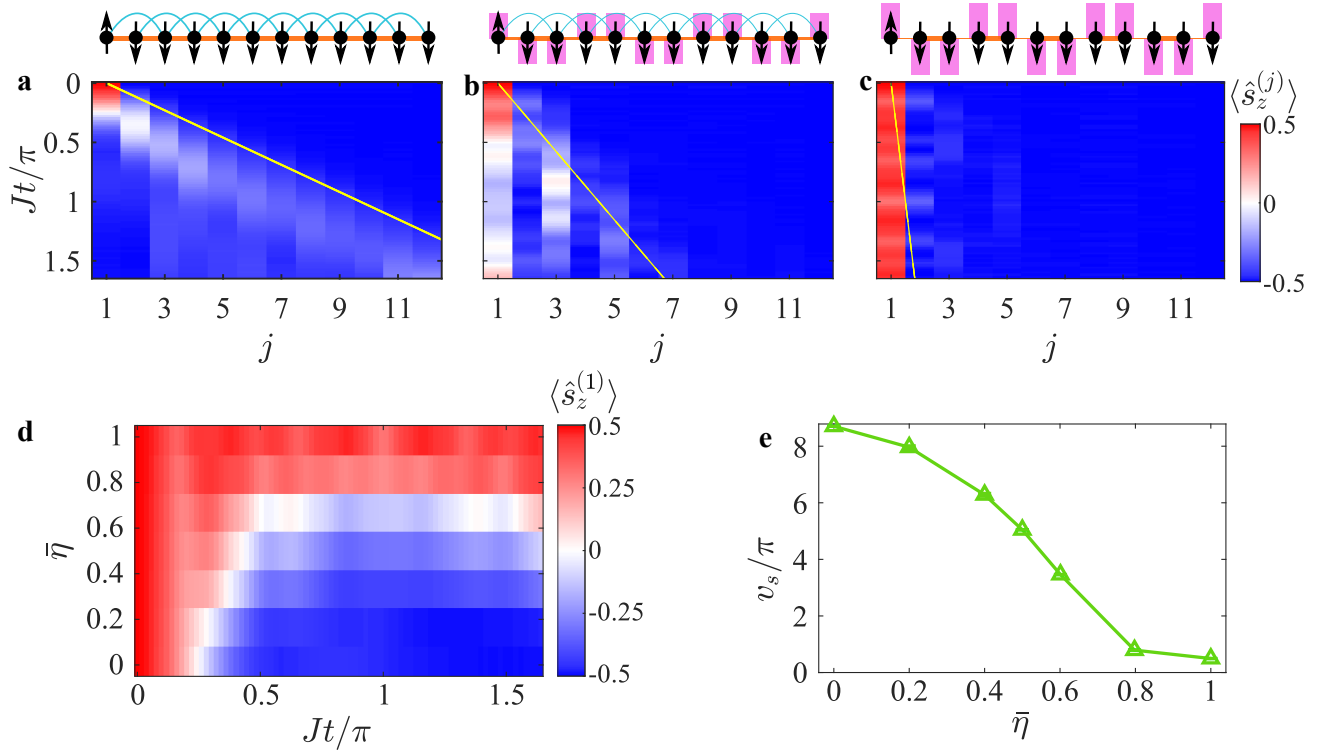
However, the term \mathcal{J}_{LR} couples $|\psi_0\rangle$ to excited states $|\psi_n\rangle_L |\psi_m\rangle_R$ with energy $\epsilon_n + \epsilon_m$. These

excited states are defined as spin waves $|\psi_n\rangle_L = 2\sum_{j\in L}\psi_{n,j}^L\hat{s}_-^{(j)}|\uparrow\rangle_L$ and $|\psi_n\rangle_R = 2\sum_{j\in R}\psi_{n,j}^R\hat{s}_+^{(j)}|\downarrow\rangle_R$, with energies given by $\mathcal{J}_{L(R)}\psi_n^{L(R)} = \epsilon_n\psi_n^{L(R)}$. The coupling strength between the initial domain wall state and these excited spin-wave states is given by $2\sum_{ij}(\mathcal{J}_{LR})_{i\in L,j\in R}\psi_{n,i}^L\psi_{n,j}^R$. For the case of short-range interaction and strong dimerization, this coupling is stronger when n and m are edge-states on the boundary between each of the sides, explaining the coherent oscillation observed in Fig. 4b. When long-range terms are introduced, long-range couplings are activated between the initial state and spin-wave states n and m in the bulk, explaining the spread of excitations along both sides of the chain.

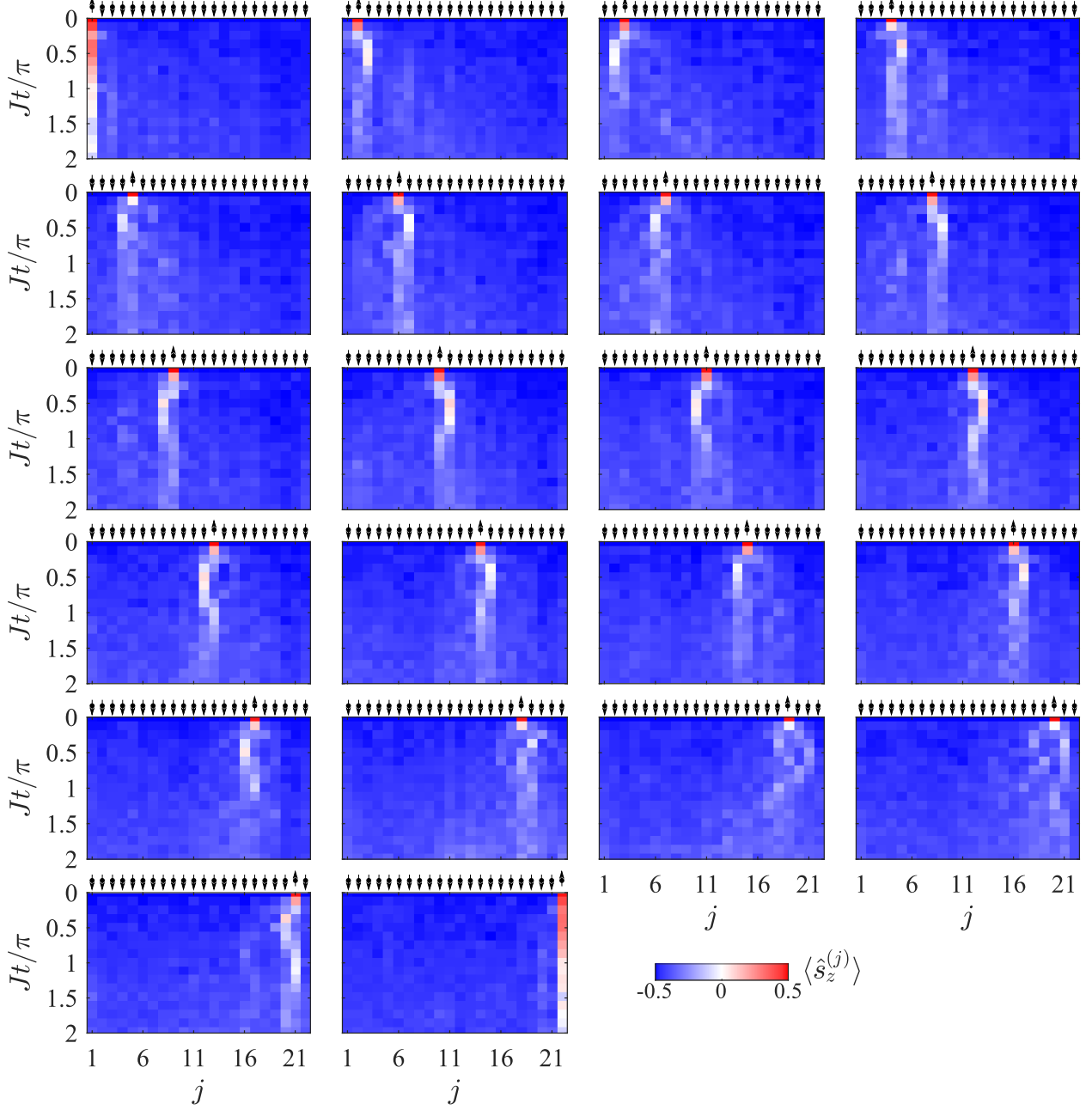
NUMERICAL SIMULATIONS AND ANALYSIS

We numerically simulate the Unitary dynamics of the $L = 12$ crystal corresponding to the full time-dependent Hamiltonian $H(t) = H_{XX} + H_Z(t)$ using the experimental parameters described in Methods. We calculate the mode participation matrix elements by solving the Laplace equation assuming the trapping potential described above, from which we find the positions of the ions. Then through linearization we determine the mode participation matrix elements, used for the calculation of the J_{ij} matrices. We represent the spin matrices, the Hamiltonian, and the quantum spin state using the sparse package in Matlab, and solve the Unitary evolution using standard ordinary differential equations (ODE45) solver.

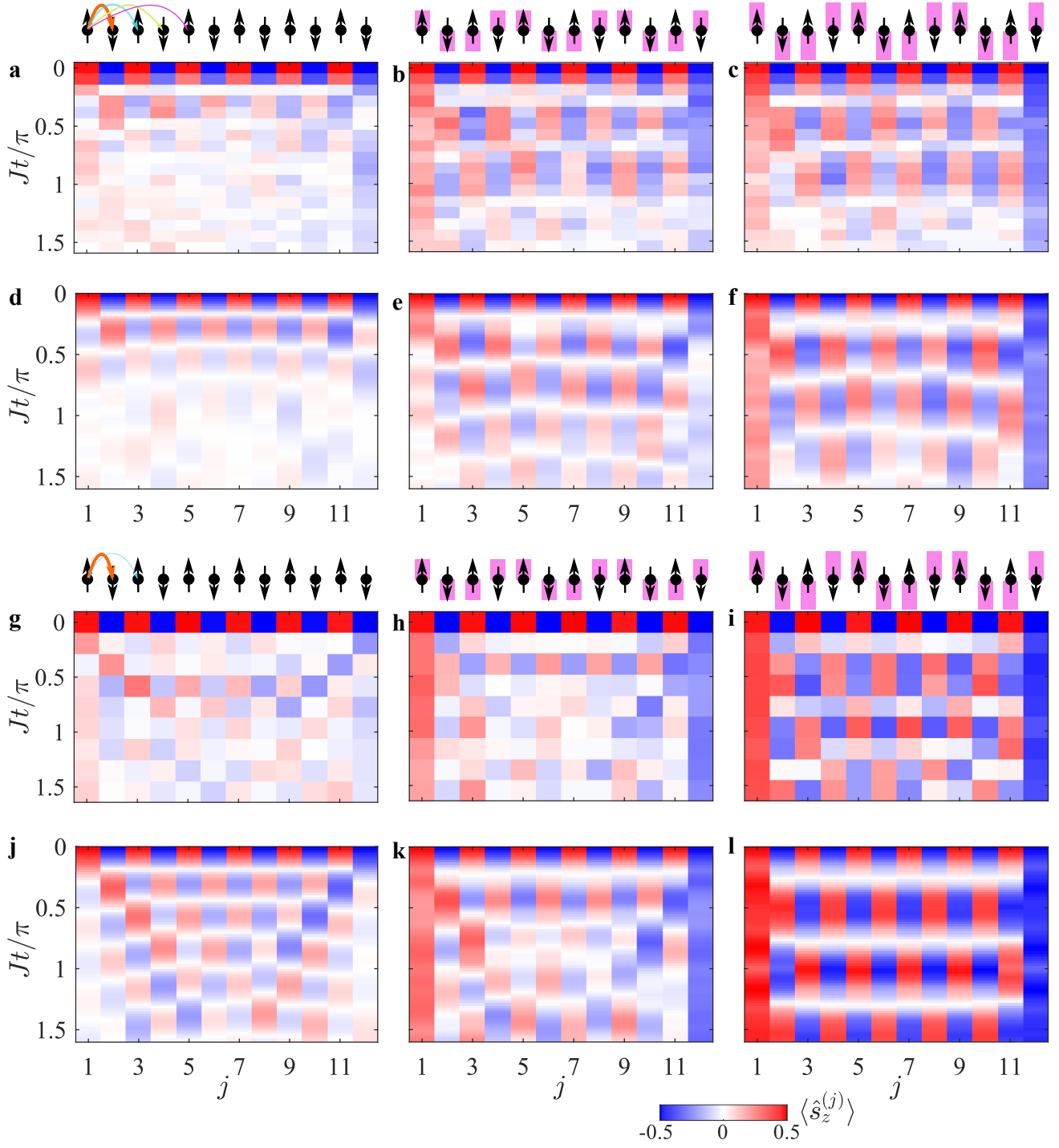
To quantify the thermalization process due to interaction, we compute the thermalization rate as the inverse of the slope of the linear line connecting the regions with magnetization above and below the equilibrium value of $\langle s_z^{(j)} \rangle = \frac{1}{2L}$ for $L = 12$. We then use a line of $\tau = (j - 1)/v_s$ to fit the boundary in the image, where j is the ion index and $\tau = Jt/\pi$ is the evolution time. The fitted slope is presented as a yellow line in Fig. 1 (d, e, and f) and Extended Data Fig. 1 (a, b, and c). Dashed lines show the values for the 95% confidence interval of the fit.



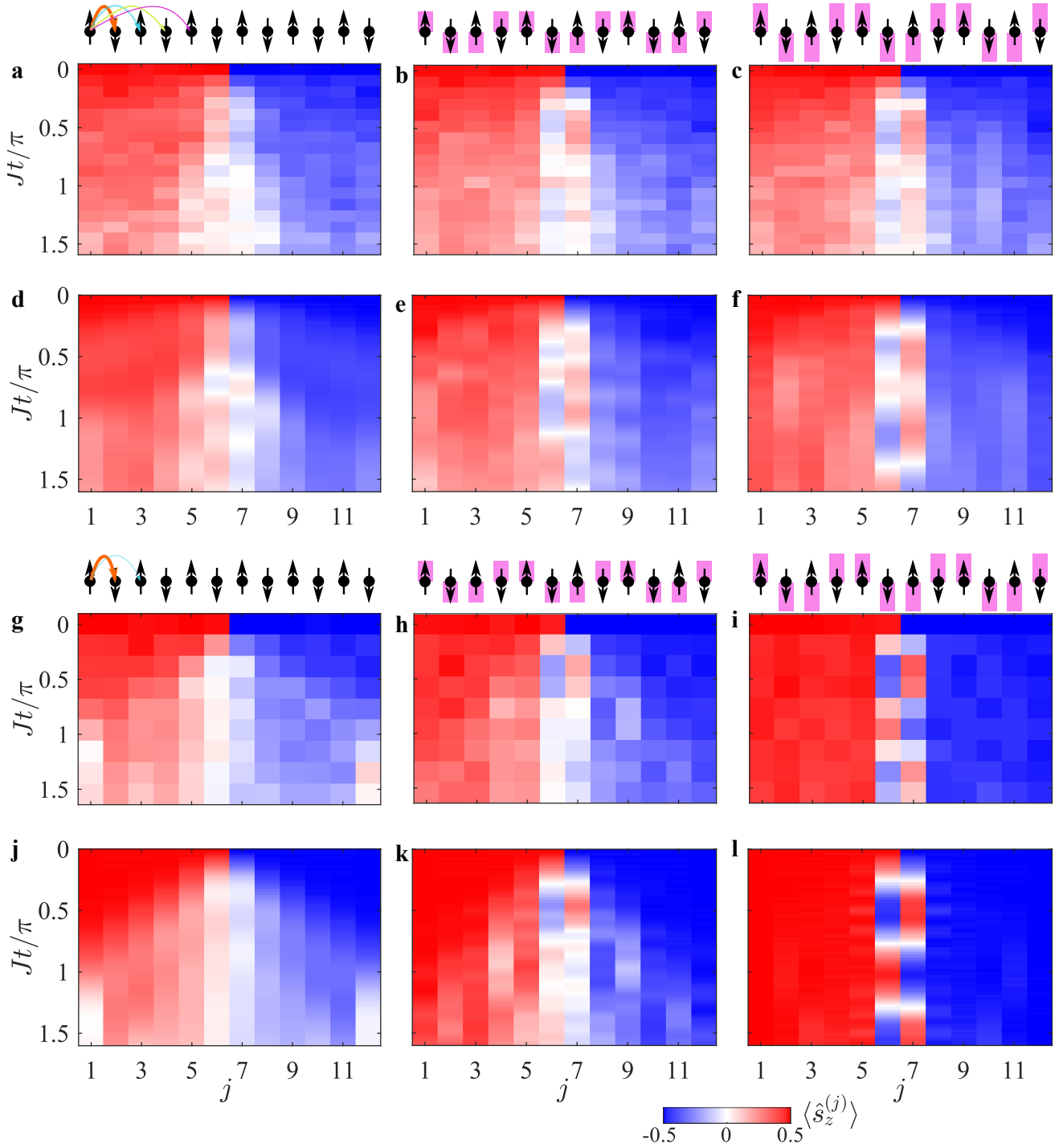
Extended Data Fig. 1. **Numerical calculation of edge-excitation.** We numerically calculated the evolution of a single spin excitation at $j = 1$ for a $L = 12$, reproducing numerically the measurements presented in Fig. 1d-h.



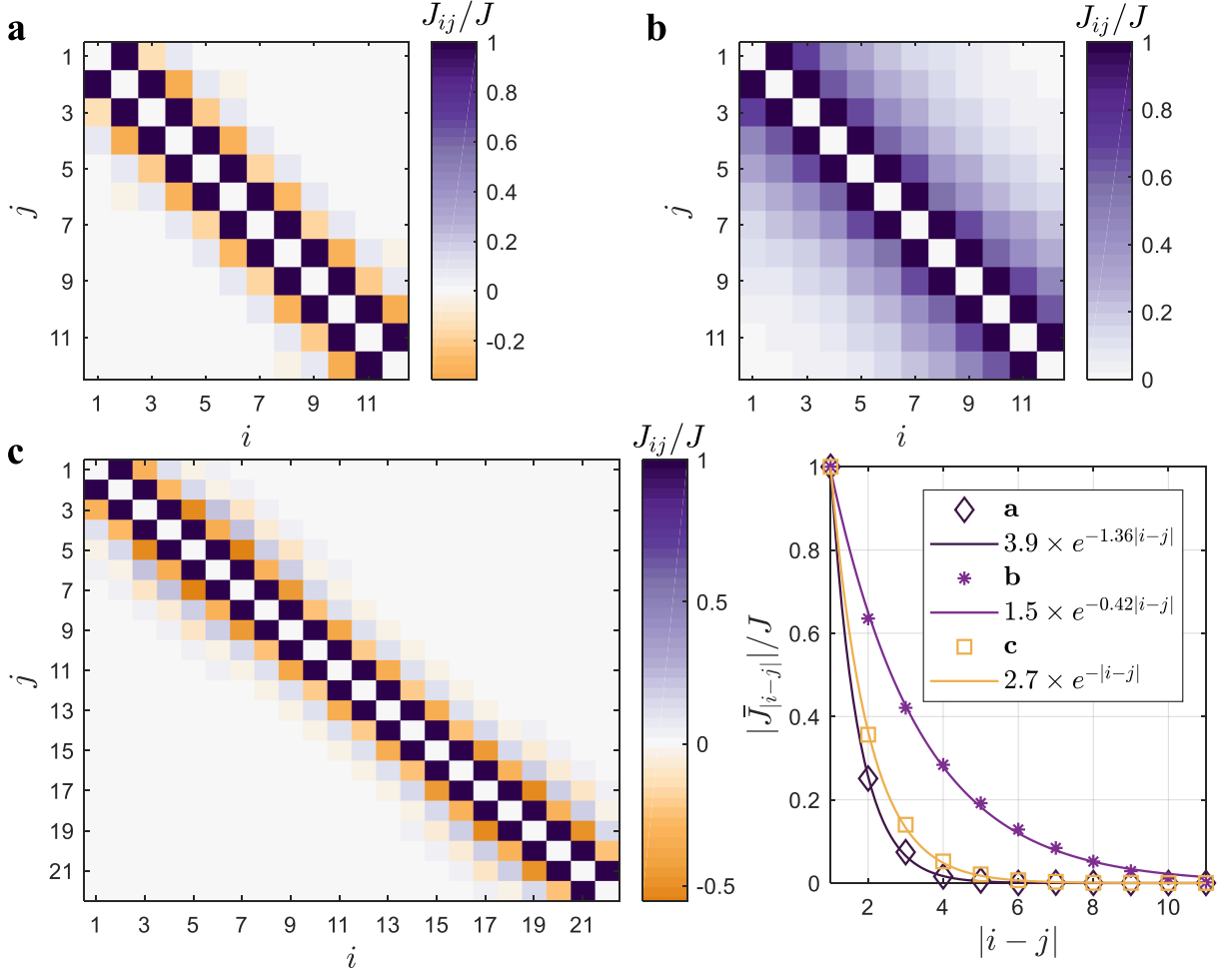
Extended Data Fig. 2. **Single-Spin Excitation in an $L = 22$ Crystal.** Evolution of a single spin excitation over time for strong Floquet modulation with $\bar{\eta} = 0.8$. $\hbar J$ represents the average nearest-neighbor spin bond energy absent the Floquet drive. Each subplot, denoted as **a-v**, corresponds to one of the 22 experiments where the j th site is initially excited, with $1 \leq j \leq 22$. Rectangular yellow box highlights the data which is used to construct the late-time-average spin $\bar{s}_{z,j}$ presented in **2c**. The mean late-time-averaged excitation of the crystal \bar{s}_z (grey line in Fig. **2c**) is independently extracted for each configuration by averaging over all spins in the crystal $\bar{s}_z = \frac{1}{11} \int_{1.5}^2 \langle \hat{s}_z^{(n)}(\tau) \rangle d\tau$ with $\tau = Jt/\pi$ where the sum goes over all $1 \leq n \leq 22$ spins in the crystal.



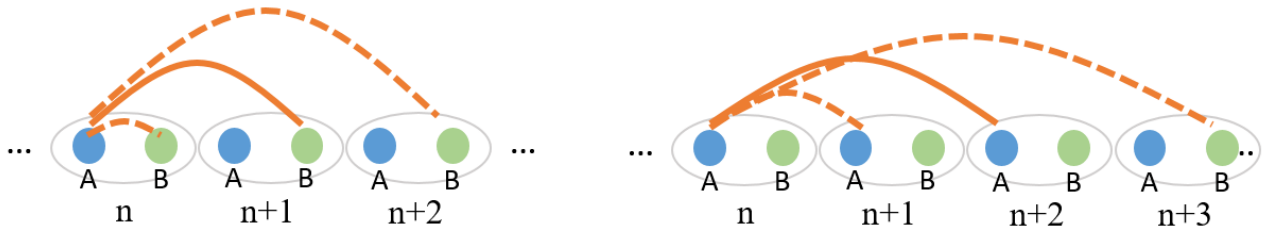
Extended Data Fig. 3. **Evolution of staggered spin state.** We initialize the $L = 12$ crystal in the Néel spin state $|\uparrow\downarrow\uparrow\downarrow \dots \uparrow\downarrow\rangle$ along the z axis and present the experimentally measured evolution for **a-c** long-range spin-spin interaction, **g-i** short range spin-spin interaction. The numerically calculated evolution for the same configurations is depicted for the long range interaction in **d-f** and for short range interaction in **j-l**. **a,d,g,j** absent the Floquet drive ($\bar{\eta} = 0$), the spins thermalize quickly as excitations hop. In the presence of Floquet fields, $\bar{\eta} = 0.6$ in **b,e,h,k** and $\bar{\eta} = 1$ in **c,f,i,l**, the thermalization is suppressed and neighboring sites exchange excitations more efficiently while the edges remain isolated. For long range interaction, the suppression of thermalization is partial, and cannot be explained with a minimal model including only free-fermionic terms (see text).



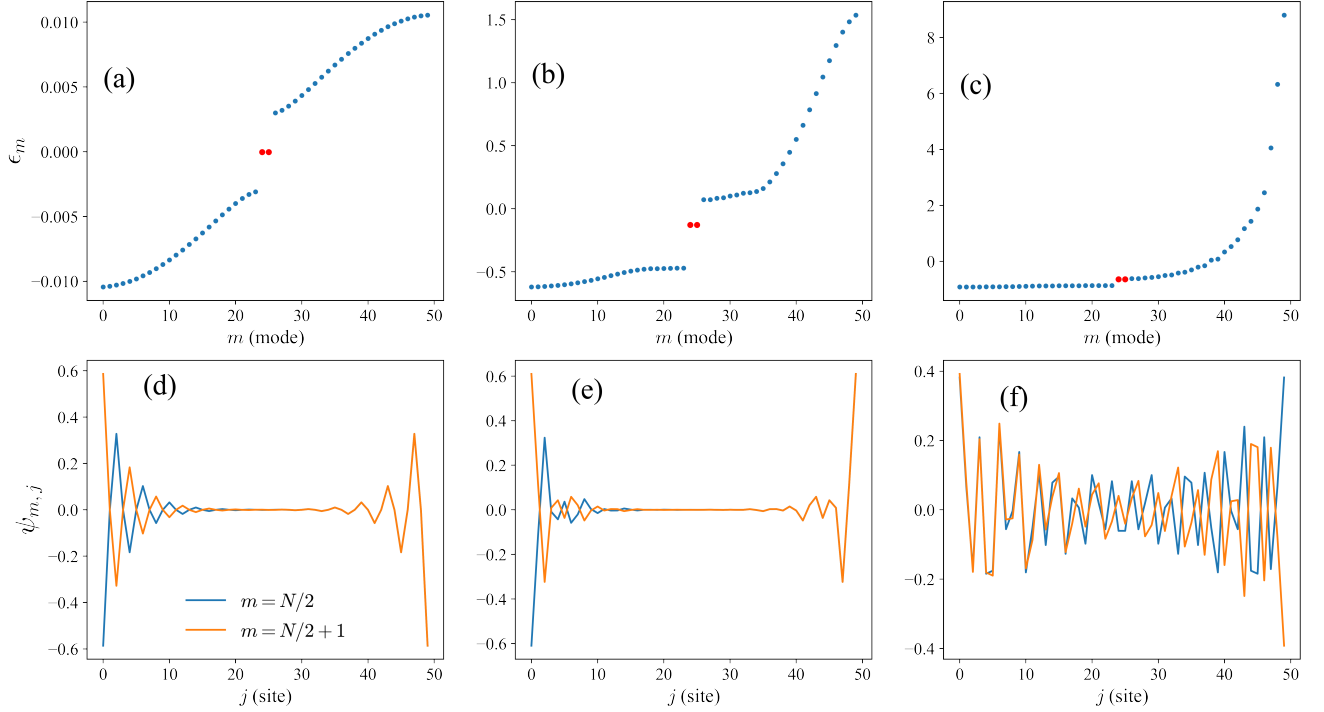
Extended Data Fig. 4. **Evolution of domain walls.** We initialize the $L = 12$ crystal in the two-domain state $|\uparrow\uparrow\uparrow\uparrow\uparrow\downarrow\downarrow\downarrow\downarrow\downarrow\rangle$ along the z axis and present the experimentally measured evolution for **a-c** long-range spin-spin interaction, **g-i** short range spin-spin interaction. The numerically calculated evolution is depicted for the long range interaction in **d-f** and for short range interaction in **j-l**. **a,d,g,j** absent the Floquet drive ($\bar{\eta} = 0$), the spins thermalize quickly as excitations hop through the boundary. In the presence of Floquet fields, $\bar{\eta} = 0.6$ in **b,e,h,k** and $\bar{\eta} = 1$ in **c,f,i,l**, the thermalization is suppressed and spins at the boundary between the two domains exchange excitations more efficiently.



Extended Data Fig. 5. **Calculated Spin-Spin Interaction Matrix.** **a-b** calculated interaction matrix for the $L = 12$ crystal. **a**, Short-range interaction. **b**, Long-range interaction. **c**, The interaction matrix for the $L = 22$ spin crystal. The staggered sign in **a,c** originates from the detuning near the zig-zag phonon modes, while the positive sign in **b** results from detuning near the center of mass mode. These matrices are calculated using Eq. 2 and the parameters provided in the text. **d** Average bond strength between spins i and j at a distance $|i - j|$ for the three configurations, normalized by the average nearest neighbor bond strength J . Exponential fits provide approximations for the interaction range.



Extended Data Fig. 6. **Sub-lattice structure of the long-range SSH model.** The dimerization pattern of long-range couplings among different sublattices (left), and within the same sublattice (right) for the topologically non-trivial case $\phi = \frac{3\pi}{4}$. Lines represent the Dimerization parameter \bar{D} (left) and D (right); see Eqs. (5-6). Weak bonds, suppressed by the Floquet fields and weighted by a dimerization parameter $j_0(\bar{\eta}z_0)$ are shown as dashed lines, while strong unsuppressed bonds are shown as continuous lines.



Extended Data Fig. 7. **Sub-lattice structure of the long-range SSH model.** We consider the eigensystem of the interaction matrix, $\mathcal{J}\psi_m = \epsilon_m\psi_m$ in the presence of inversion symmetry. **(a - c)** Eigenvalues of \mathcal{J} with interaction range $\xi = 0.1$ **(a)**, $\xi = 2$ **(b)** and $\xi = 6$ **(c)** [see Eq. (9)], in a crystal of $L = 50$ spins, moderate dimerization $\bar{\eta} = 0.6$ and $\phi = \frac{3\pi}{4}$. **(d - f)** Wavefunction $\psi_{m,j}$ of mid-gap states with index $m = N/2, N/2 + 1$ for the values of ξ listed above. At shorter interaction ranges these states are localized near the edges, while at longer range they are strongly mixed with the bulk.

-
- [1] C.-K. Chiu, J. C. Teo, A. P. Schnyder, and S. Ryu, *Reviews of Modern Physics* **88**, 035005 (2016).
- [2] C. Nayak, S. H. Simon, A. Stern, M. Freedman, and S. D. Sarma, *Reviews of Modern Physics* **80**, 1083 (2008).
- [3] J. E. Moore, *Nature* **464**, 194 (2010).
- [4] M. Z. Hasan and C. L. Kane, *Reviews of modern physics* **82**, 3045 (2010).
- [5] W.-P. Su, J. R. Schrieffer, and A. J. Heeger, *Physical review letters* **42**, 1698 (1979).
- [6] W.-P. Su, J. Schrieffer, and A. Heeger, *Physical Review B* **22**, 2099 (1980).
- [7] A. J. Heeger, S. Kivelson, J. R. Schrieffer, and W.-P. Su, *Reviews of Modern Physics* **60**, 781 (1988).
- [8] G. Jotzu, M. Messer, R. Desbuquois, M. Lebrat, T. Uehlinger, D. Greif, and T. Esslinger, *Nature* **515**, 237 (2014).
- [9] M. Atala, M. Aidelsburger, J. T. Barreiro, D. Abanin, T. Kitagawa, E. Demler, and I. Bloch, *Nature Physics* **9**, 795 (2013).
- [10] M. Hafezi, S. Mittal, J. Fan, A. Migdall, and J. Taylor, *Nature Photonics* **7**, 1001 (2013).
- [11] T. Ozawa, H. M. Price, A. Amo, N. Goldman, M. Hafezi, L. Lu, M. C. Rechtsman, D. Schuster, J. Simon, O. Zilberberg, *et al.*, *Reviews of Modern Physics* **91**, 015006 (2019).
- [12] M. Jalali Mehrabad, S. Mittal, and M. Hafezi, *Phys. Rev. A* **108**, 040101 (2023).
- [13] S. De Léséleuc, V. Lienhard, P. Scholl, D. Barredo, S. Weber, N. Lang, H. P. Büchler, T. Lahaye, and A. Browaeys, *Science* **365**, 775 (2019).
- [14] I. Pogorelov, T. Feldker, C. D. Marciniak, L. Postler, G. Jacob, O. Kriegelsteiner, V. Podlesnic, M. Meth, V. Negnevitsky, M. Stadler, *et al.*, *PRX Quantum* **2**, 020343 (2021).
- [15] R. Yao, W.-Q. Lian, Y.-K. Wu, G.-X. Wang, B.-W. Li, Q.-X. Mei, B.-X. Qi, L. Yao, Z.-C. Zhou, L. He, *et al.*, *Physical Review A* **106**, 062617 (2022).
- [16] J. G. Bohnet, B. C. Sawyer, J. W. Britton, M. L. Wall, A. M. Rey, M. Foss-Feig, and J. J. Bollinger, *Science* **352**, 1297 (2016).
- [17] C. Monroe, W. C. Campbell, L.-M. Duan, Z.-X. Gong, A. V. Gorshkov, P. W. Hess, R. Islam, K. Kim, N. M. Linke, G. Pagano, P. Richerme, C. Senko, and N. Y. Yao, *Rev. Mod. Phys.* **93**, 025001 (2021).
- [18] P. Nevado and D. Porras, *Physical Review A* **93**, 013625 (2016).
- [19] Z.-X. Gong, M. F. Maghrebi, A. Hu, M. Foss-Feig, P. Richerme, C. Monroe, and A. V. Gorshkov, *Physical Review B* **93**, 205115 (2016).
- [20] L. Feng, O. Katz, C. Haack, M. Maghrebi, A. V. Gorshkov, Z. Gong, M. Cetina, and C. Monroe, [arXiv:2211.01275](https://arxiv.org/abs/2211.01275) (2022).
- [21] M. S. Rudner and N. H. Lindner, *Nature reviews physics* **2**, 229 (2020).
- [22] N. H. Lindner, G. Refael, and V. Galitski, *Nature Physics* **7**, 490 (2011).
- [23] O. Katz, G. Refael, and N. H. Lindner, *Physical Review B* **102**, 155123 (2020).
- [24] Y. Wang, H. Steinberg, P. Jarillo-Herrero, and N. Gedik, *Science* **342**, 453 (2013).
- [25] J. W. McIver, B. Schulte, F.-U. Stein, T. Matsuyama, G. Jotzu, G. Meier, and A. Cavalleri, *Nature physics* **16**, 38 (2020).
- [26] J. Zhang, P. W. Hess, A. Kyprianidis, P. Becker, A. Lee, J. Smith, G. Pagano, I.-D. Potirniche, A. C. Potter, A. Vishwanath, *et al.*, *Nature* **543**, 217 (2017).
- [27] S. Choi, J. Choi, R. Landig, G. Kucsko, H. Zhou, J. Isoya, F. Jelezko, S. Onoda, H. Sumiya, V. Khemani, *et al.*, *Nature* **543**, 221 (2017).
- [28] P. Kiefer, F. Hakelberg, M. Wittemer, A. Bermúdez, D. Porras, U. Warring, and T. Schaetz, *Physical Review Letters* **123**, 213605 (2019).
- [29] P. Nevado, S. Fernández-Lorenzo, and D. Porras, *Physical Review Letters* **119**, 210401 (2017).
- [30] P. L. W. Maunz, *High optical access trap 2.0.*, Tech. Rep. (Sandia National Lab.(SNL-NM), Albuquerque, NM (United States), 2016).
- [31] L. Egan, D. M. Debroy, C. Noel, A. Risinger, D. Zhu, D. Biswas, M. Newman, M. Li, K. R. Brown, M. Cetina, *et al.*, *Nature*, 1 (2021).
- [32] O. Katz, L. Feng, A. Risinger, C. Monroe, and M. Cetina, *Nature Physics*, 1 (2023).
- [33] S. Olmschenk, K. C. Younge, D. L. Moehring, D. N. Matsukevich, P. Maunz, and C. Monroe, *Phys. Rev. A* **76**, 052314 (2007).
- [34] L. N. Egan, *Scaling Quantum Computers with Long Chains of Trapped Ions*, Ph.D. thesis, University of Maryland, College Park (2021).
- [35] B. Pérez-González, M. Bello, A. Gómez-León, and G. Platero, *Phys. Rev. B* **99**, 035146 (2019).
- [36] G. van Miert, C. Ortix, and C. M. Smith, *2D Materials* **4**, 015023 (2016).
- [37] Z.-Q. Jiao, S. Longhi, X.-W. Wang, J. Gao, W.-H. Zhou, Y. Wang, Y.-X. Fu, L. Wang, R.-J. Ren, L.-F. Qiao, and X.-M. Jin, *Phys. Rev. Lett.* **127**, 147401 (2021).